Supplementary Information (SI) for Journal of Materials Chemistry A.

Synergistic Promotion of Oxygen Reduction Electrocatalysis by Chlorine Incorporation in Biomass-derived S/N Co-doped Carbon

Ming Li, ‡[a] Haolin Chang, ‡[a] Chenxin Fan[a], Chen Wang[a], Liyuan Gong*[a], and Shuo Dou*[a]

State Key Laboratory of Utilization of Woody Oil Resource, Key Laboratory of Bio-Based Material Science and Technology of the Ministry of Education, Northeast Forestry University, Harbin, 150040, China

1 Experimental Section

1.1 Chemicals and materials

The sulfate lignin used in this study was purchased from UPM Biochemicals. Sodium chloride, urea, iron(III) nitrate nonahydrate, nickel(II) nitrate hexahydrate, ammonium fluoride, potassium hydroxide, and zinc acetate were all acquired from Aladdin Reagent Co., Ltd. Nafion117 solution was obtained from Innochem Co., Ltd. platinum on carbon (20 wt% loading) was procured from Beijing Inno-chem Technology Co., Ltd. Ruthenium oxide (Ru≥75 wt%) was procured from Suzhou Sinero Technology Co., Ltd. Unless otherwise stated, all chemicals were of analytical grade and were used without any additional purification. Ultrapure water was used throughout the experiment.

1.2 Preparation of Cl-SNC

First, 1.4 g of sulfate lignin was placed in a 100 mL round-bottom flask, followed by the sequential addition of 50 mL of deionized water, 1 g of NaCl, and 1 g of urea. A magnetic heating stirrer was used to heat and stir the mixture at 90°C, allowing the components to fully dissolve and subsequently precipitate. After the water had completely evaporated, the solid was transferred to a vacuum drying oven and dried at 60°C for 12 hours. The solid sample was then thoroughly ground for 8 minutes using a high-energy ball mill. Next, the ground solid sample was placed in a tube furnace. Under an argon atmosphere, the temperature was raised to 900°C at a heating rate of 5°C·min^{-1} and maintained for 2 hours. After heating, the sample was subjected to vacuum filtration and washed extensively with water to remove NaCl. Finally, the sample was placed in a vacuum drying oven at 60°C for 12 hours to obtain the Cl-SNC catalyst.

1.3 Preparation of SNC, SC, Porous SNC and NiFe LDH

The preparation process for SNC only omits the addition of NaCl, with all other steps remaining the same.

The preparation process for SC involves omitting the addition of urea based on the SNC procedure, with all other steps kept unchanged.

The preparation process for Porous SNC involves adding 1.2 g of KOH during the solution mixing stage on the basis of the SNC procedure, with all other steps remaining

the same.

Preparation of NiFe LDH: First, 2 mmol of $Ni(NO_3)_2 \cdot 6H_2O$ and 1 mmol of $Fe(NO_3)_3 \cdot 9H_2O$ were completely dissolved in 35 mL of deionized water. Then, while stirring, 8 mmol of NH_4F and 12 mmol of urea were added, and stirring was continued for 2 hours. After complete dissolution, the resulting mixture was transferred into a Teflon-lined stainless-steel autoclave. Subsequently, a hydrothermal reaction was carried out at 120°C for 12 hours. After naturally cooling to room temperature, the product was washed multiple times with ethanol and deionized water to remove surface-deposited catalyst residues. Finally, the sample was placed in a vacuum drying oven at 60°C for 12 hours to obtain the NiFe LDH catalyst.

2. Physical characterizations

The morphology of the samples was examined by scanning electron microscopy (SEM; Zeiss Supra 55) and high-resolution transmission electron microscopy (HRTEM; JEOL JEM-F200, Japan). Raman spectra were collected using a HORIBA Scientific LabRAM HR Evolution system. Powder X-ray diffraction (XRD) patterns were recorded over a 2θ range of 5–80° with Cu Kα radiation on a PANalytical X'Pert Pro diffractometer (PANalytical B.V.). X-ray photoelectron spectroscopy (XPS) analyses were performed on a Thermo electron spectrometer (ThermoFisher) to probe the bonding states. The specific surface areas were determined by the Brunauer–Emmett–Teller (BET) method from N_2 adsorption/desorption isotherms measured at 77 K using an automated adsorption analyzer (Micromeritics ASAP 2460).

3. Electrochemical characterizations

In a standard three-electrode testing system, the oxygen reduction reaction performance of the electrocatalyst was measured using a CHI 760E electrochemical workstation from Shanghai Chenhua Instrument Co., Ltd. A platinum sheet was employed as the counter electrode, and an Ag/AgCl electrode served as the reference electrode. The working electrode was prepared as follows: 5 mg of the catalyst was dispersed in 1 mL of a mixed solution consisting of 990 µL of isopropanol and 10 µL of Nafion solution, followed by ultrasonic treatment for 30 minutes to form a uniformly dispersed catalyst ink. Then, 20 µL of this ink was evenly drop-cast onto the surface of

a glassy carbon electrode with a diameter of 5 mm. The working electrode for the commercial Pt/C (20 wt%) catalyst was prepared using the same procedure. Cyclic voltammetry tests were conducted in a 0.1 M KOH electrolyte, which was saturated with either N_2 or O_2, over a potential range of 0.2–0.8 V (vs. Ag/AgCl) at a scan rate of 50 mV s^{-1}. Electrochemical impedance spectroscopy measurements were performed with a frequency range of 10,000 to 0.01 Hz and an AC amplitude of 5 mV. The double-layer capacitance was calculated from CV tests conducted in a 0.1 M KOH solution within a potential window of 1.15–1.25 V at varying scan rates. The long-term stability of the catalysts was assessed using chronoamperometry. Measurements were carried out using the rotating ring-disk electrode technique over a rotation speed range of 400 to 2025 rpm (scan rate: 10 mV s^{-1}). To evaluate stability, continuous long-term tests were performed on Cl-SNC and Pt/C catalysts at a constant potential of 0.6 V (vs. Ag/AgCl) in an O_2-saturated 0.1 M KOH electrolyte.

The following computation was used to determine the theoretical Levich slope (B):

$$B = 0.62nFC_{O_2}D_{O_2}^{2/3}v^{-1/6} \quad (1)$$

where n, C_{O_2}, F, v, and D_{O_2} denote the transfer electron number, the oxygen concentration (solution) (1.2×10^{-6} mol cm^{-3}), the Faradaic constant (96485 C mol^{-1}), the kinematic viscosity of the 0.1 M KOH (0.01 cm^2 s^{-1}) and the oxygen diffusion coefficient (1.9×10^{-5} cm^2 s^{-1}).

Furthermore, the kinetic characteristics of the oxygen reduction reaction were investigated using a rotating ring-disk electrode (RRDE) in an O_2-saturated 0.1 M KOH solution at a scan rate of 5 mV·s^{-1}. Based on the linear sweep voltammetry (LSV) data collected by the RRDE at a rotation speed of 1600 rpm, the hydrogen peroxide yield and electron transfer number were calculated using the following formulas:

$$n = 4 \times \frac{I_D}{I_D + I_R/N} \quad (2)$$

$$H_2O_2(\%) = 200 \times \frac{I_R/N}{I_D + I_R/N} \quad (3)$$

The I_D is the disk current and I_R is the ring current, respectively. The N represents

the current collection efficiency equaled to 0.37 of the RRDE in our experimental system.

4 DFT calculation

All the calculations are performed in the framework of the density functional theory with the projector augmented plane-wave method, as implemented in the Vienna ab initio simulation package [1]. The generalized gradient approximation proposed by Perdew, Burke, and Ernzerhof is selected for the exchange-correlation potential [2]. The Grimme D3 correction using a coordination number dependent dispersion correction [3]. The cut-off energy for plane wave is set to 450 eV. The energy criterion is set to 10^{-5} eV in iterative solution of the Kohn-Sham equation. A vacuum layer of 15 Å is added perpendicular to the sheet to avoid artificial interaction between periodic images. The Brillouin zone integration is performed using a 4×2×2 k-mesh [4]. All the atoms were relaxed until the residual forces on the atoms have declined to less than 0.02 eV/Å. Spin polarization is included in the calculations. The Free energy changes (ΔG) of reaction intermediates could be calculated by the following:

$$\Delta G = \Delta E + \Delta E_{ZPE} - T\Delta S$$

where ΔE is the adsorption energy on the cluster surface from DFT calculations. The ΔE_{ZPE} and ΔS are the difference for the zero-point energy and entropy. The zero-point energy and entropy are calculated at the standard conditions corresponding to the pressure of 101325 Pa (~1 bar) of H_2 at the temperature of 298.15 K.

5 Liquid Zinc–air battery measurements

The core structure of a zinc-air battery consists of three parts: the cathode, the anode, and the electrolyte. During the preparation of the cathode, the catalyst is first uniformly dispersed in an aqueous system, followed by the addition of a Nafion membrane solution to form a catalyst slurry with a concentration of 5 $mg \cdot mL^{-1}$. This slurry is evenly coated onto a carbon paper substrate and allowed to dry naturally, ensuring a catalyst loading of 1 $mg \cdot cm^{-2}$ on the carbon paper. For anode preparation, the surface of a zinc sheet is polished with sandpaper to remove the oxide layer, and the resulting clean zinc sheet is directly used as the anode. The electrolyte is a mixed solution of 6 $mol \cdot L^{-1}$ KOH and 0.2 $mol \cdot L^{-1}$ $Zn(Ac)_2$. Finally, using a zinc-air battery mold

provided by Changsha Spring Company, the aforementioned cathode, anode, and electrolyte are assembled into a complete liquid zinc-air battery system.

Supplementary Figures:

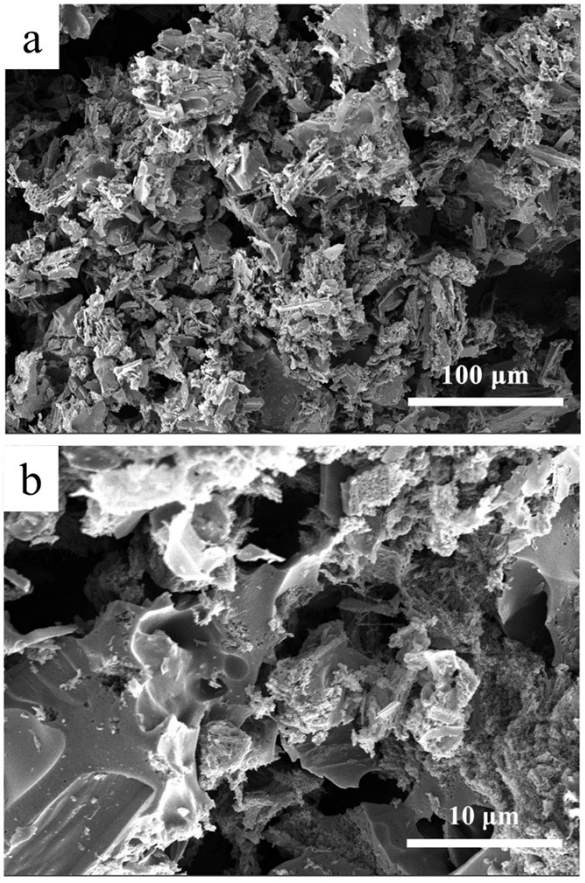

Figure S1. (a, b) SEM images of SNC.

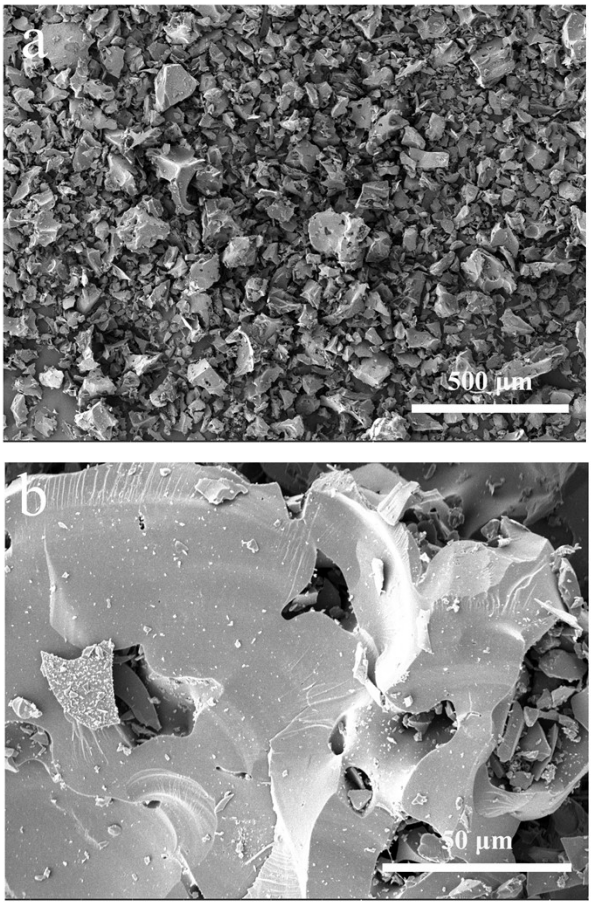

Figure S2. (a, b) SEM images of SC.

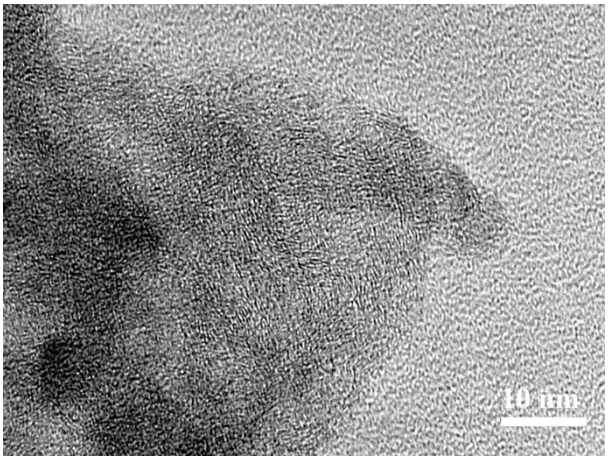

Figure S3. HRTEM image of Cl-SNC.

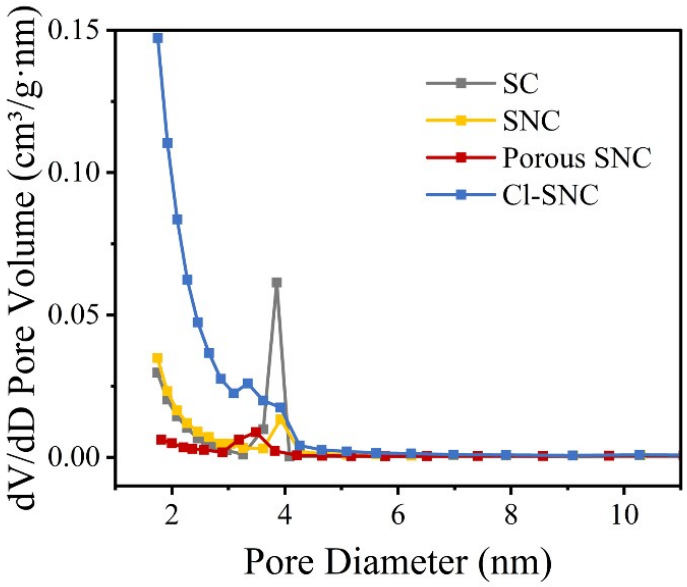

Figure S4. Barrett-Joyner-Halenda curves of Cl-SNC, SNC, Porous SNC and Cl-SNC.

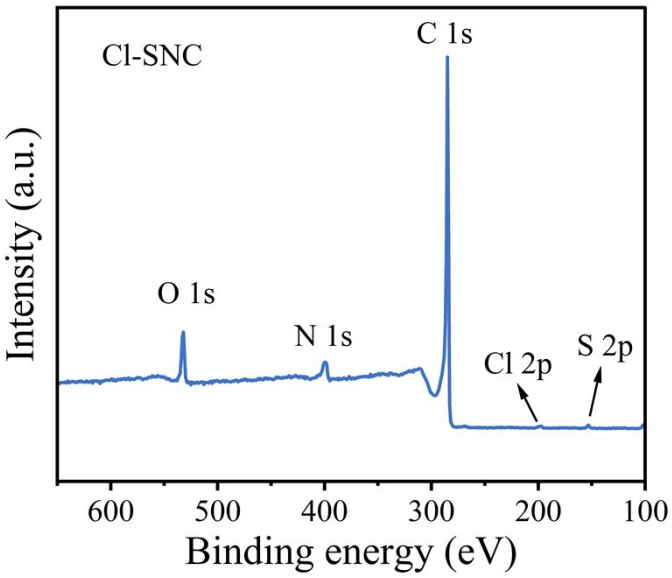

Figure S5. XPS survey spectrum of Cl-SNC.

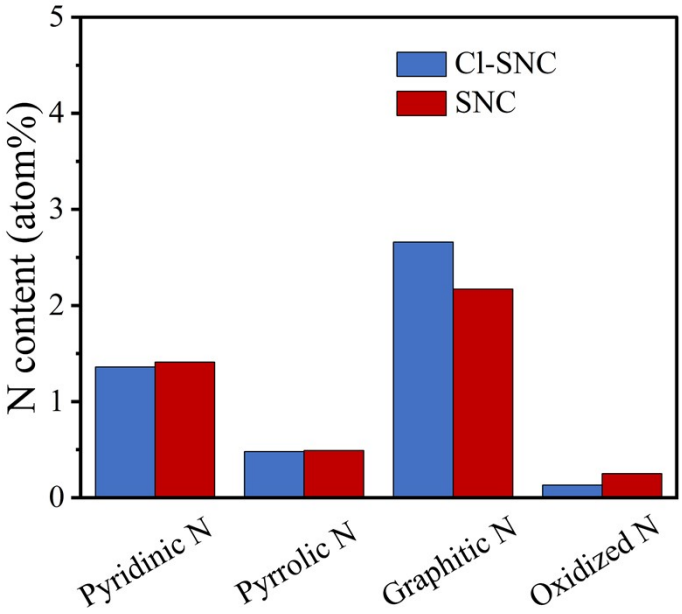

Figure S6. Content of N-doped configuration.

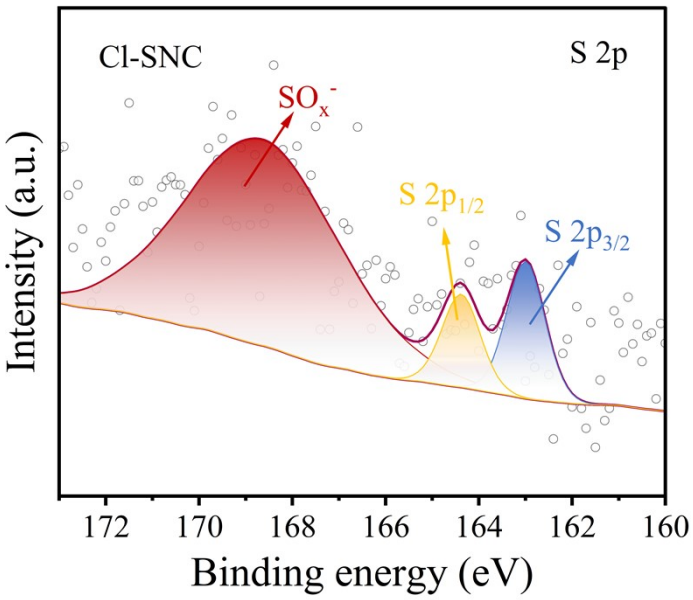

Figure S7. High-resolution XPS spectrum of S 2p.

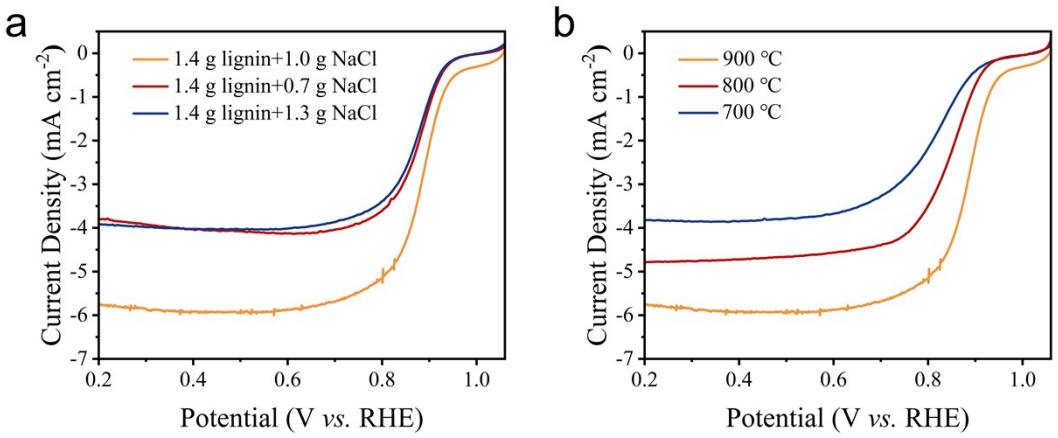

Figure S8. LSV curves for the ORR of electrocatalysts prepared at different lignin-to-NaCl ratios (a) and carbonization temperatures (b)

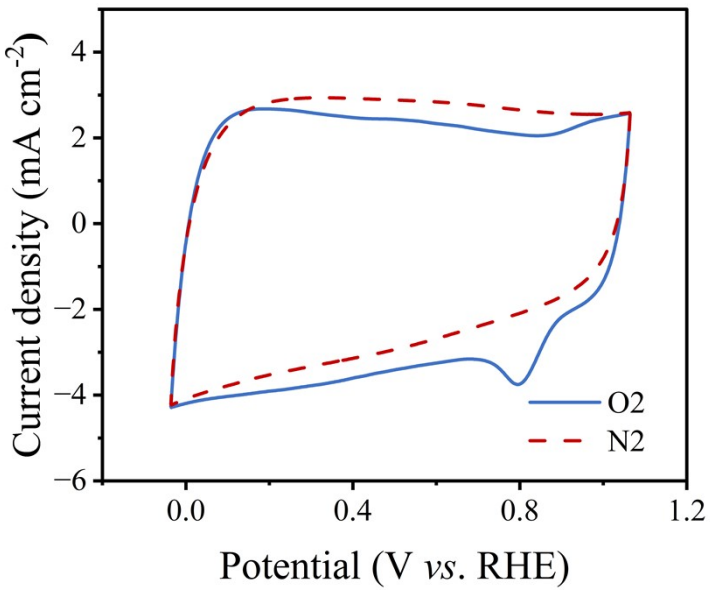

Figure S9. Cyclic voltammetry (CV) curves of the Cl-SNC electrocatalyst collected in N_2- and O_2-saturated 0.1 M KOH electrolyte

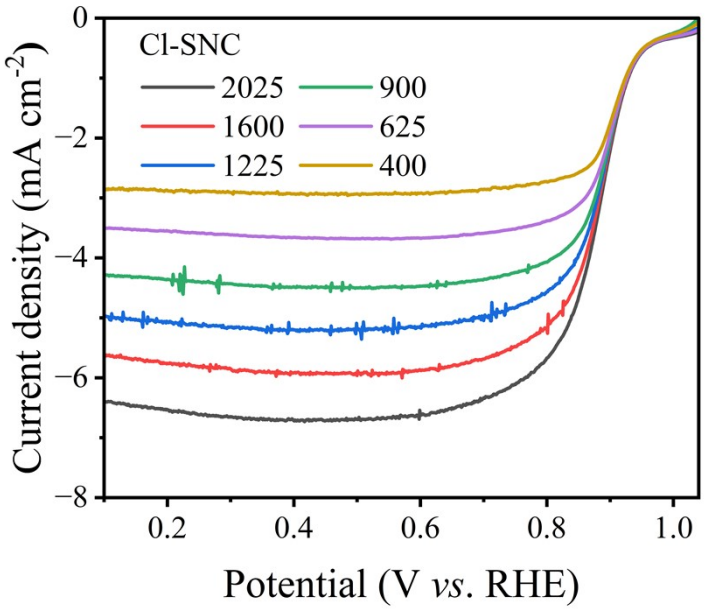

Figure S10. The LSV curves of Cl-SNC with various rotating rates

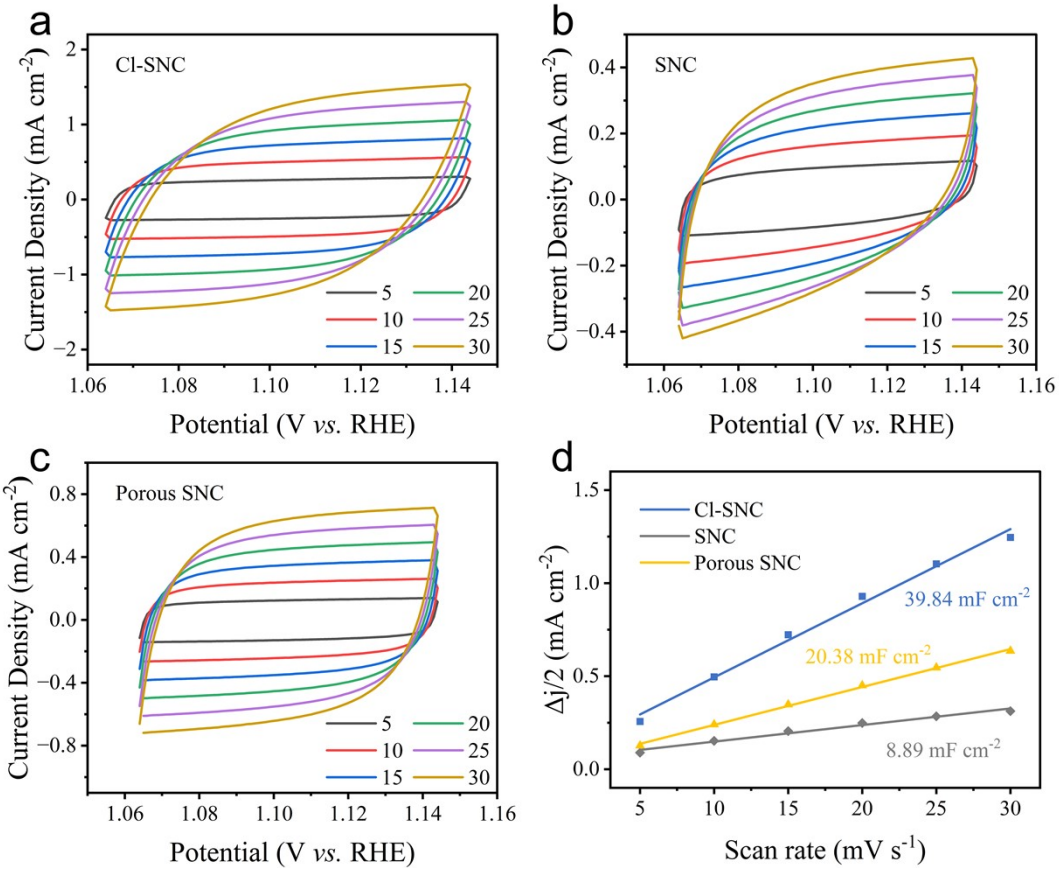

Figure S11. CV curves of (a) Cl-SNC, (b) SNC and (c) Porous SNC at various scan rates from 5 to 30 mV s^{-1}. (d) The summarized double layer capacitance (C_{dl}) of Cl-SNC, SNC and Porous SNC.

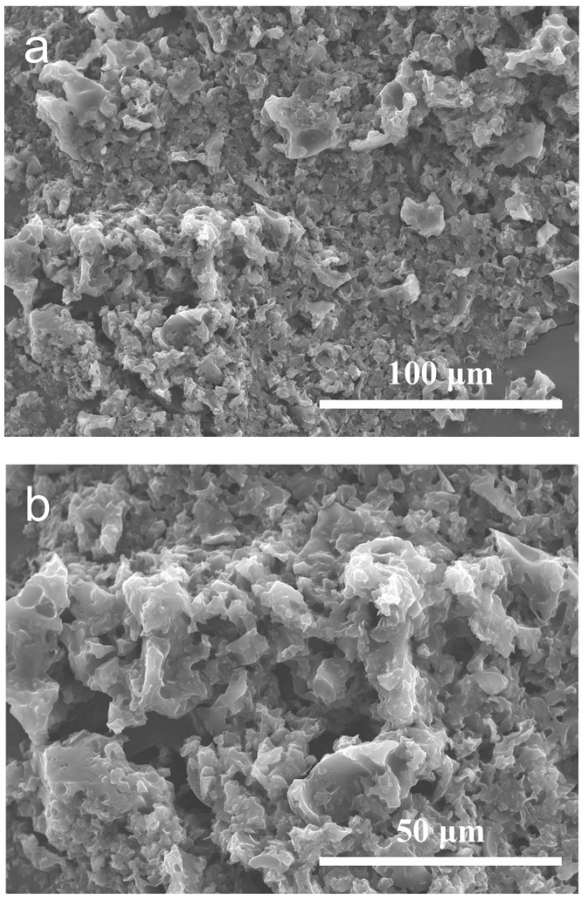

Figure S12. (a, b) SEM images of Cl-SNC after testing.

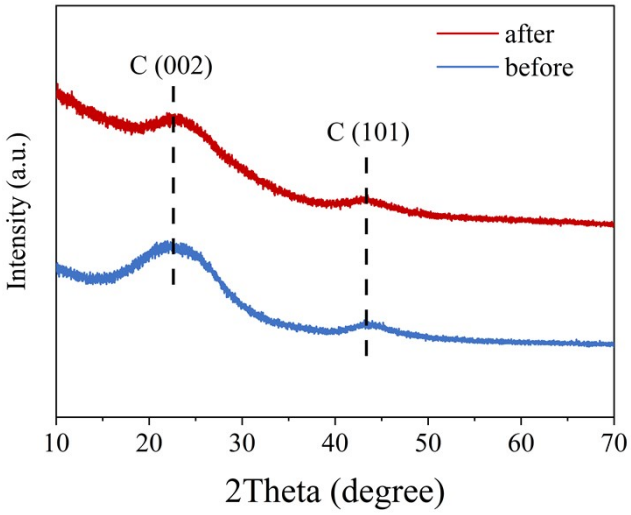

Figure S13. XRD patterns of Cl-SNC before and after testing.

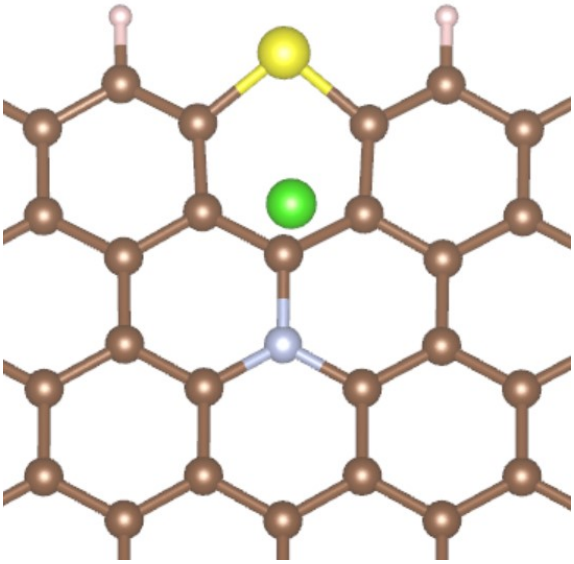

Figure S14. DFT-optimized structures of Cl at different carbon sites.

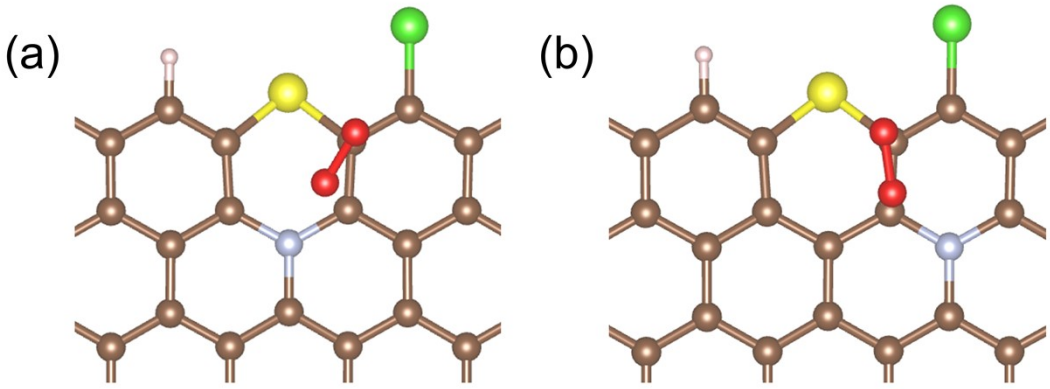

Figure S15. Cl-SNC adsorption configuration for O_2

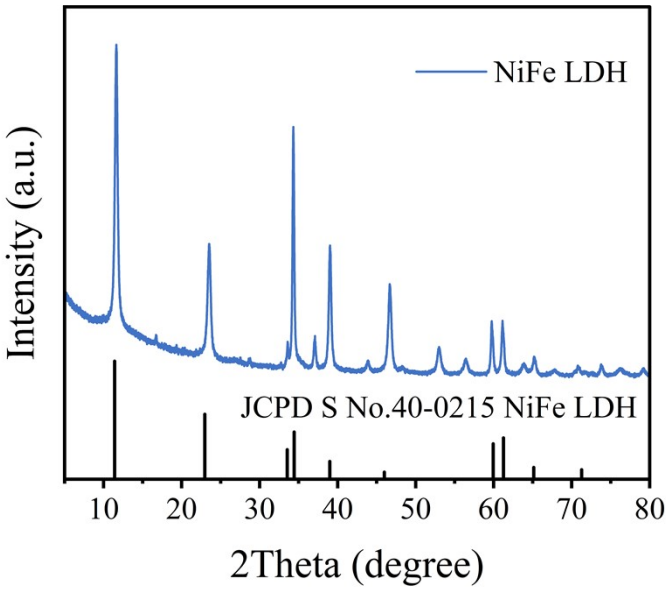

Figure S16. XRD pattern of NiFe LDH, with black lines representing the reference standard card.

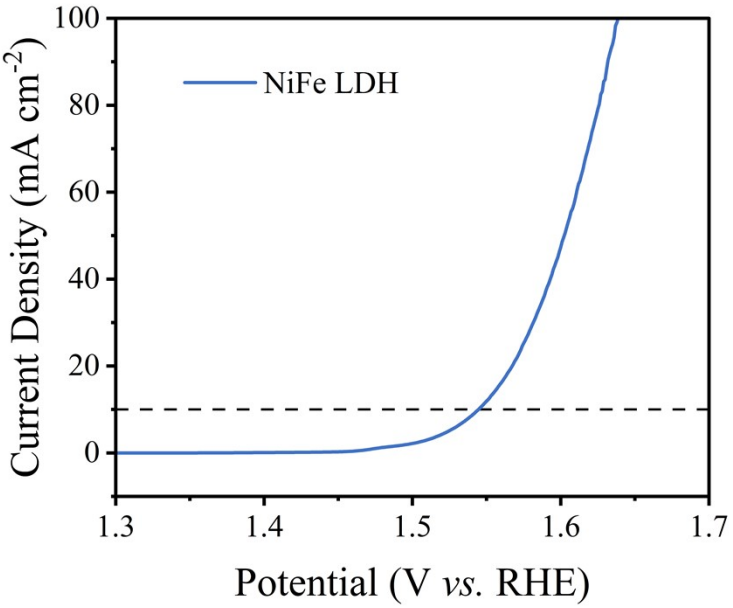

Figure S17. Polarization curves for OER

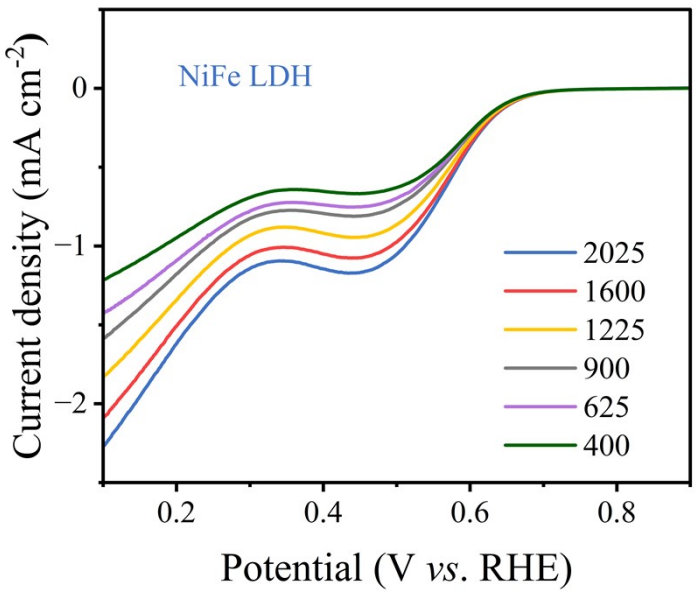

Figure S18. Polarization curves for ORR.

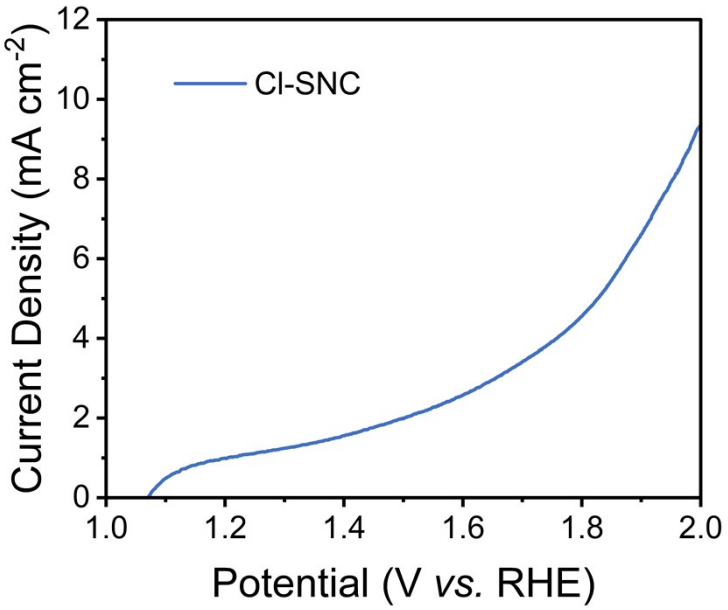

Figure S19. OER LSV curves of Cl-SNC

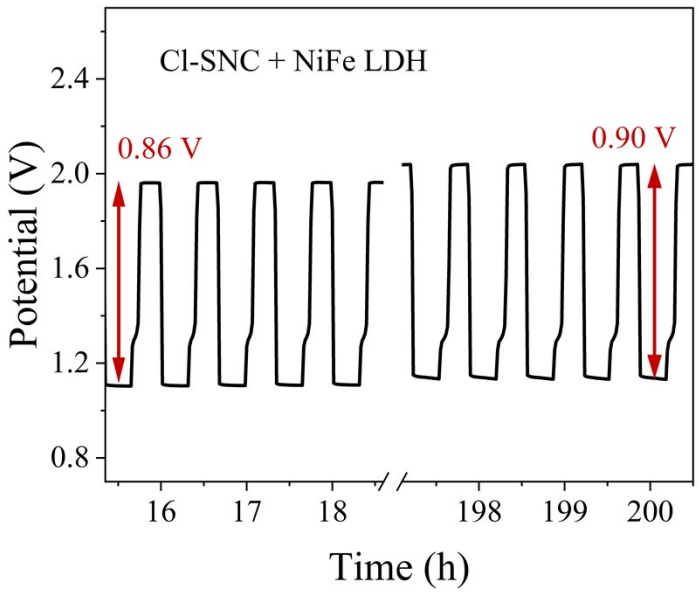

Figure S20. Galvanostatic discharge/charge curves of Cl-SNC + NiFe LDH at 49 ~50 h and 419 ~420 h, respectively.

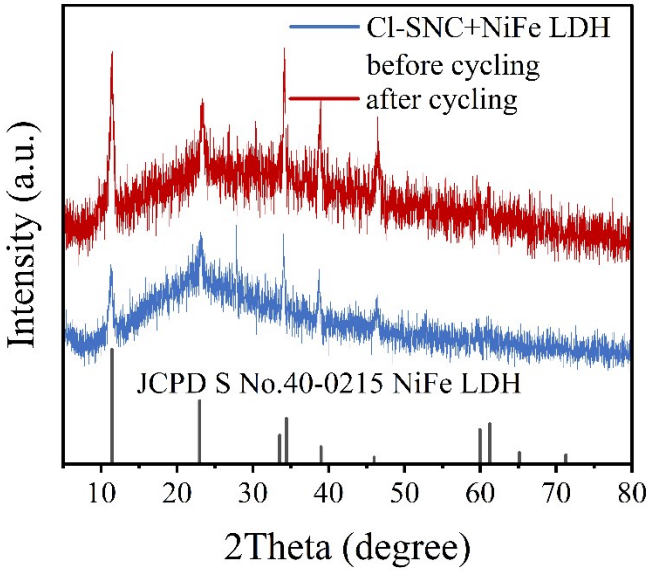

Figure S21. XRD patterns of Cl-SNC+NiFe LDH before and after Zn-air battery charge-discharge cycling

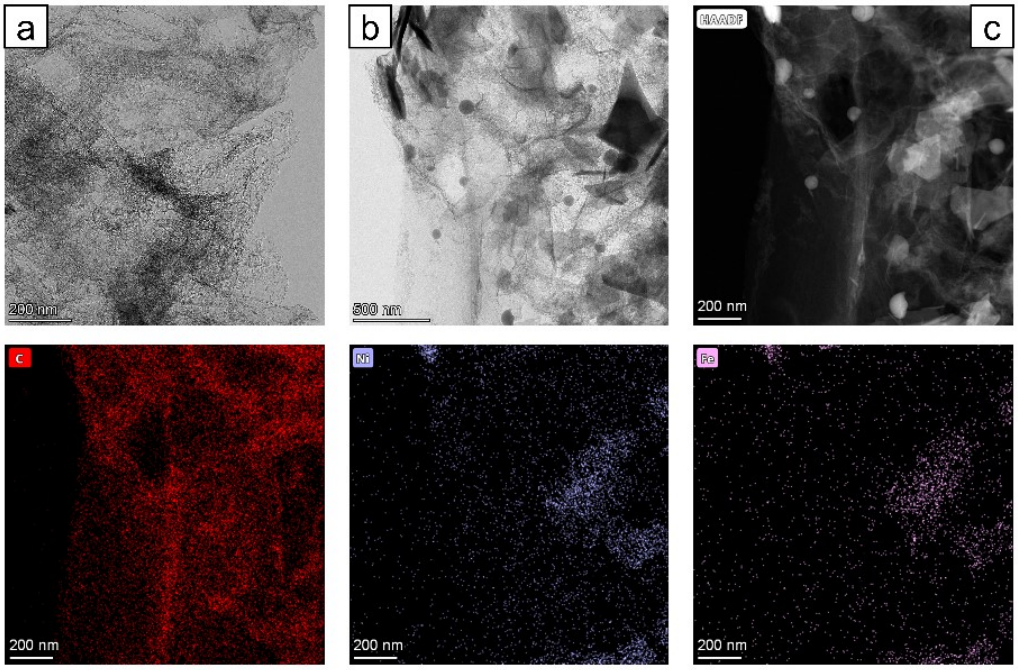

Figure S22. (a, b) TEM images and EDS mapping image (c) of Cl-SNC+NiFe LDH

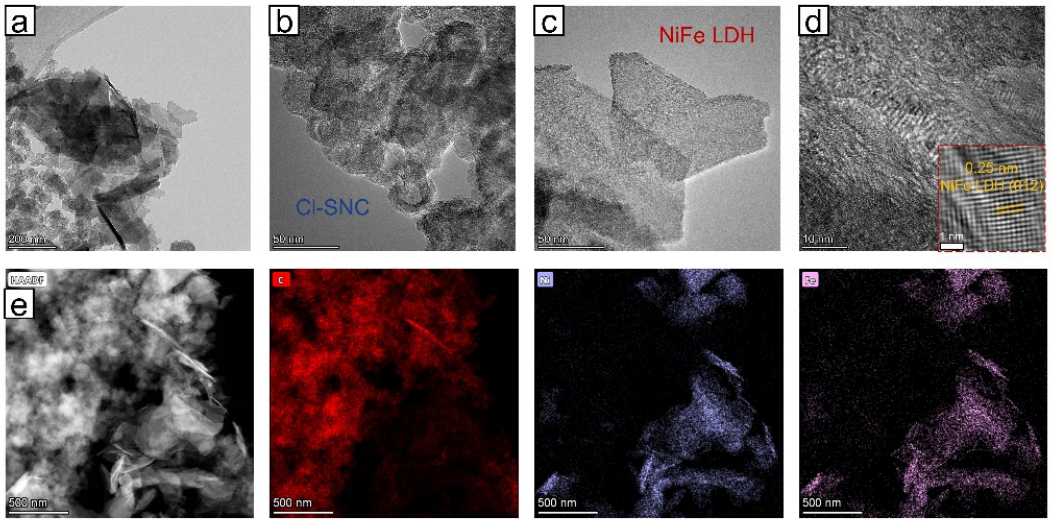

Figure S23. (a-c) TEM image, (d) HRTEM and EDS mapping images (e) of Cl-SNC+NiFe LDH catalyst after Zn-air battery charge-discharge cycling.

Table S1 ORR catalytic performance comparison between Cl-SNC and other metal-free carbon-based catalysts.

Catalyst	E_{onset} (V vs. RHE)	$E_{1/2}$ (V vs. RHE)	Ref.
NDPC-1000	0.97	0.87	[5]
mf-pClNC	1.02	0.91	[6]
NPC-950	1.06	0.88	[7]
NPC-4-1100-Zn	1.00	0.85	[8]
NPCS-900	0.99	0.87	[9]
NCNAS	1.01	0.91	[10]
CTS/Cl/S	0.95	0.85	[11]
Cl-SNC	**1.05**	**0.89**	**This work**

Table S2 Comparison of the performance of liquid Zn-air batteries assembled with Cl-SNC and other reported biomass-derived carbon-based catalysts.

Catalyst	Power density ($mW \cdot cm^{-2}$)	Specific capacity ($mAh\ g_{Zn}^{-1}$)	Cyclability/ current density (h)/($mA\ cm^{-2}$)	Ref.
Cl-SNC	160	1179.2	200 5	**This work**
SA-Cu@NCA	191.3	779.3	100 5	[12]
CTS/Cl/S	180	815	300 10	[11]
N/E-HPC-900	192.7	801	110 10	[13]
SAC-Fe-WPC	152	763.8	200 5	[14]
NSCW-900	149	757.5	125 5	[15]

References

[1] Kresse, G.; Joubert, D. From ultrasoft pseudopotentials to the projector augmented- wave method. Physical Review B 1999, 59, 1758-177.
[2] Perdew, J. P.; Burke, K.; Ernzerhof, M. Generalized gradient approximation made simple. Physical Review Letters 1996, 77, 3865-3868.
[3] Grimme, S., Antony, J., Ehrlich, S. & Krieg, H. A consistent and accurate ab initio parametrization of density functional dispersion correction (DFT-D) for the 94 elements H-Pu. J. Chem. Phys. 132, 154104 (2010).
[4] H.J. Monkhorst, J.D. Pack, Special points for Brillouin-zone integrations, Phys. Rev. B. 13 (1976) 5188–5192.
[5] Jin J, Qiao X, Cheng F, et al. Direct synthesis of interconnected N, S-codoped porous exfoliated carbon nanosheets as advanced electrocatalysts for oxygen reduction reaction, Carbon, 2017, 122: 114-121.
[6] Karaaslan M, Lin L, Ko F, et al. Carbon aerogels from softwood Kraft lignin for high performance supercapacitor electrodes, Frontiers in Materials, 2022, 9: 894061.
[7] Yang L, Liu H, Qiao Z, et al. Highly active and durable metal-free carbon catalysts for anion-exchange membrane fuel cells, Advanced Energy Materials, 2023, 13(20): 2204390.
[8] Li Z, Ji S, Liu H, et al. Constructing asymmetrical coordination microenvironment with phosphorus-incorporated nitrogen-doped carbon to boost bifunctional oxygen electrocatalytic activity, Advanced Functional Materials, 2024, 34(18): 2314444.
[9] Zhu J, Xiao M, Song P, et al. Highly polarized carbon nano-architecture as robust metal-free catalyst for oxygen reduction in polymer electrolyte membrane fuel cells, Nano Energy, 2018, 49: 23-30.
[10] Ren G, Chen S, Zhang J, et al. N-doped porous carbon spheres as metal-free electrocatalyst for oxygen reduction reaction, Journal of Materials Chemistry A, 2021, 9(9): 5751-5758.
[11] C. Lin, X. Cao, L. Wang, M. Cai, R. Ma, J. Ma, S/Cl Co-doped biomass-derived carbon electrocatalysts: Low ΔE of 0.58 V for ORR/OER and application in high-performance zinc-air batteries, Nano Energy, 2026, 150: 111791.
[12] Z. Chen, L. Zhong, Z. Chen, H. Zhuo, X. Zhao, H. Lai, T. Li, W. Yang, Z. Liu, H. Zhang, E. Iwuoha, K. Ocakoglu, X. Peng, Reconstructed wood carbon aerogel with single-atom sites for flexible Zn-air Batteries, ACS Nano, 2025, 19: 23859–23868.
[13] X. Peng, L. Zhang, Z. Chen, L. Zhong, D. Zhao, X. Chi, X. Zhao, L. Li, X. Lu, K. Leng, C. Liu, W. Liu, W. Tang, K.P. Loh, Hierarchically porous carbon plates derived from wood as bifunctional ORR/OER electrodes, Adv Mater, 2019, 31: e1900341.
[14] L. Zhong, C. Jiang, M. Zheng, X. Peng, T. Liu, S. Xi, X. Chi, Q. Zhang, L. Gu, S. Zhang, G. Shi, L. Zhang, K. Wu, Z. Chen, T. Li, M. Dahbi, J. Alami, K. Amine, J. Lu, Wood carbon based single-atom catalyst for rechargeable Zn–air batteries, ACS Energy Letters, 2021, 6: 3624–3633.
[15] S. Zhang, Z. Chen, Z. Xiong, Z. Wang, Z. Zhao, Z. Xue, K. Li, K. Wang, B. Hui, Electronic structure regulation of carbon atoms from wood for enhancing Zn–air battery performances, Journal of Materials Chemistry A, 2025, 13: 2198–2207.